Immobilization of Co nanoparticles into N-doped carbon nanotube on g-C$_3$N$_4$ via coordination-polymerization integrated strategy for efficient H$_2$ evolution reaction at all pH values

Xiang Yan [a], Chao Zhang [a,b,*], Jinguang Hu [c], Yuming Zhou [d], Zhiguo Lv [a,**]

[a] State Key Laboratory Base for Eco-chemical Engineering, College of Chemical Engineering, Qingdao University of Science and Technology, Qingdao 266042, China
[b] Guangxi Key Laboratory of Petrochemical Resource Processing and Process Intensification Technology, Guangxi University, Nanning 530004, China
[c] Department of Chemical & Petroleum Engineering, Schulich School of Engineering, Calgary, Alberta T2N 1N4, Canada
[d] School of Chemistry and Chemical Engineering, Southeast University, Jiangsu Optoelectronic Functional Materials and Engineering Laboratory, Nanjing 211189, China

ARTICLE INFO

ABSTRACT

Constructing Co-based carbon nanotubes/g-C$_3$N$_4$ structure via integrated strategy remains a challenge in cobalt-based electrocatalysis. We firstly proposed a coordination-polymerization integrated strategy for the preparation of Co@N-CNT@g-C$_3$N$_4$ with efficient hydrogen evolution reaction at all pH values. In Co@N-CNT@g-C$_3$N$_4$, Co nanoparticles were encapsulated in the tip of carbon nanotubes and carbon nanotubes grew on g-C$_3$N$_4$ to bridge Co particles and g-C$_3$N$_4$. More importantly, Co particles, carbon nanotubes, and g-C$_3$N$_4$ were assembled simultaneously skillfully to construct a closely integrated interface, thereby enhancing electron transfer efficiency. Electrochemical tests showed that the structure has high catalytic activity, with overpotentials of 61, 145, and 170 mV in 1 M KOH, 0.5 M H$_2$SO$_4$ and 1.0 M phosphate buffer saline (PBS), respectively, to drive 10 mA cm^{-2}. Additionally, the Gibbs free energy for hydrogen adsorption (ΔG_H*) on the Co surface of Co@N-CNT@g-C$_3$N$_4$ was only $-$ 0.13 eV, which was conducive to H$_2$ formation.

1. Introduction

The electrocatalytic hydrogen evolution reaction (HER) has become a promising and eco-friendly method to generate hydrogen via water splitting [1,2]. In order to achieve large-scale hydrogen evolution, it is imperative to ameliorate reaction overpotentials via the utilization of high-efficiency catalysts [3,4]. In this regard, transition metal-based catalysts, particularly cobalt nanoparticles, have emerged as promising candidates due to their excellent catalytic activity, abundance, and low cost [5–7]. Nonetheless, various impediments must be tackled to further raise the HER efficacy of Co-based catalysts. The immobilization of cobalt nanoparticles (Co NPs) on an appropriate support matrix is a critical facet to augment the overall electroconductivity [8–10]. Carbon-based materials, encompassing graphene, g-C$_3$N$_4$ and carbon nanotubes (CNTs), demonstrate a remarkable aptitude for reactants adsorption, functional group enrichment (which facilitate metal particle loading), anti-corrosion, and electron transfer efficiency [11–13]. And

thus, it has been widely used in cobalt-based electrocatalysis. Up to now, numerous investigations have been conducted on Co/carbon materials (e.g., Co, N, S tri-doped graphene [14], Co@g-C$_3$N$_4$ [15], N-Co-S/-graphene [16] and CoSbO@CNT[17]). In comparison to other carbon materials, CNTs exhibit distinctive features. The 1D nanostructure endows CNTs with superior electron transport efficiency. Concurrently, the hollow structure of CNTs facilitates mass transport [5]. This has been corroborated by a variety of studies (e.g., Co@N-CNT [18], CoNP@N-CNTs [9], Co-NCNTs [19], and CoM@CNTs [20]). However, the overpotential is typically no less than 100 mV at a current density of 10 mA cm^{-2} in 1 M KOH electrolyte. Introducing another carbon material with closely integrated C/C heterointerface into this catalytic system may potentially lead to a significant HER enhancement. However, it is difficult to further introduce another carbon materials in Co/CNTs systems using the aforementioned catalyst preparation method, let alone constructing closely integrated C/C heterointerface.

It is thus of utmost necessity to explore a facile strategy for

* Corresponding author at: State Key Laboratory Base for Eco-chemical Engineering, College of Chemical Engineering, Qingdao University of Science and Technology, Qingdao 266042, China.
** Corresponding author.
E-mail addresses: chaozhangchem@qust.edu.cn (C. Zhang), lvzhiguo@qust.edu.cn (Z. Lv).

introducing carbon material as a support into Co/CNTs. Notably, the carbon support/Co/CNTs exhibits a hierarchical structure. The hierarchical structure can facilitate mass transfer and H$_2$ desorption [21]. Currently, g-C$_3$N$_4$ has been extensively utilized for the fabrication of hierarchical structures owing to its exceptional physical and chemical characteristics [22–25]. Only a handful of reports, such as those on NiCo@N-CNTs@g-C$_3$N$_4$ [6] and g-C$_3$N$_4$/Co@N-CNT [26], have implemented such structures and demonstrated their exceptional catalytic performance in photocatalysis. Despite the remarkable advances, there are still great challenges and improvement space for Co@N-CNTs@g-C$_3$N$_4$ catalysts: (1) The construction of Co@N-CNTs@g-C$_3$N$_4$ architectures is highly complex and generally requires multiple mixing and calcination steps; (2) The support material (g-C$_3$N$_4$) is initially prepared, followed by the grafting of Co@CNT onto g-C$_3$N$_4$. However, carbon nanotubes and g-C$_3$N$_4$ lack tight interface, which may impede effective electron transfer. By integrated construction approach, a close C/C heterointerface can be formed between CNT and g-C$_3$N$_4$, thereby enhancing electron transfer efficiency; (3) As far as I know, Co-based carbon nanotubes/g-C$_3$N$_4$ series catalysts are only utilized for photocatalysis, and its electrocatalytic performance has not been investigated. In order to address the above problems, we considered whether suitable C, N-containing compounds could be utilized in condensation to construct CNTs/g-C$_3$N$_4$ structures at the same time? At present, research has found that the photocatalytic activity of g-C$_3$N$_4$ prepared using supramolecular precursors comprising melamine-cyanuric acid has demonstrated exceptional performance as compared to that synthesized solely from melamine [27–30]. The excellent performance of g-C$_3$N$_4$ (uses supramolecular precursors) may be due to the optimized electronic structure [31,32]. Inspired by this, the utilization of cyanuric acid may lead to a breakthrough in the integrated construction of Co-based carbon nanotubes/g-C$_3$N$_4$ structures via one-step strategy.

Herein, through coordination-polymerization integrated strategy an integrated Co@N-CNT@g-C$_3$N$_4$ structure was prepared successfully for effective hydrogen evolution reaction at all pH values. The integrated Co@N-CNT@g-C$_3$N$_4$ (Co@CNT@CN) features unique Co active sites (encapsulated in the tips of CNTs), efficient electron transfer pathways (Co N-CNT → g-C$_3$N$_4$), facile mass diffusion and enhanced mechanical stability. These beneficial properties synergistically improve the catalytic performance of the HER catalyst over the wide range of pH 0–14. At an electrolyte composition of 1 M KOH, 0.5 M H$_2$SO$_4$ and 1.0 M PBS, Co@CNT@CN exhibited overpotentials of 61, 145 and 170 mV to reach a current density of 10 mA cm^{-2}, respectively. Density functional theory (DFT) calculations uncover that g-C$_3$N$_4$ diminishes the interactions between Co@CNT and H atoms, thus yielding a higher $\Delta G_H{}^*$.

2. Experimental section

2.1. Synthesis of Co@CNT@CN

The preparation of Co@CNT@CN includes two steps: (i) The synthesis of Co-imidazole coordination compound (Co-ICC) was achieved through stirring a mixture of PVP (4.320 g), 2-methylimidazole (4.720 g), cobalt nitrate (Co(NO$_3$)$_2$·6 H$_2$O, 1.746 g) and 12 mL methanol for 6 h. The resulting product was washed four times with ethanol, followed by drying at 60 °C under vacuum for 24 h. (ii) The synthesis of Co@CNT@CN via one-step thermopolymerization strategy: Co-ICC and cyanuric acid were fully ground in different proportions (Co-ICC/cyanuric acid ratio = 0.03, 0.05, 0.1, 0.15, 0.2 and 0.25) in an agate mortar and subsequent annealing at 550 °C for 4 h in nitrogen atmosphere. The corresponding samples were denoted as Co@CNT@CN-1, Co@CNT@CN-2, Co@CNT@CN-3, Co@CNT@CN-4, Co@CNT@CN-5 and Co@CNT@CN-6. Synthesis of g-C$_3$N$_4$ was conducted via direct annealing of cyanuric acid at 550 °C (under N$_2$ atmosphere) for 4 h, while Co/C was synthesized by annealing of Co-ICC at the same temperature (under N$_2$ atmosphere) for 4 h. Synthesis of M-Co@CNT@CN

and Co@CNT@CN-3 was analogous, with the substitution of cyanuric acid by an equivalent amount of melamine.

2.2. Material characterization, electrochemical measurement, DFT calculations detail

This information is in the supporting material.

3. Results and discussion

The synthetic routine of Co@CNT@CN was schematically illustrated in Fig. 1. The morphology of Co@CNT@CN was investigated by SEM. Fig. 2a-c clearly shows the even growth of CNTs on the surface of g-C$_3$N$_4$. Further observation of Fig. 2d revealed Co NPs were wrapped in the tips of CNTs. The synthesized Co@CNT@CN exhibits a hierarchical structure, which is advantageous for mass diffusion and electrolyte penetration during electrocatalytic processes. Furthermore, the morphological changes of a series of Co@CNT@CN were investigated by varying Co-ICC/cyanuric acid ratio. As evidenced by Fig. S1a, g-C$_3$N$_4$ exhibits a typical cotton-like sheet structure. When Co-ICC/cyanuric acid ratio is 0.03, many NPs initiate to appear on g-C$_3$N$_4$ surface (Fig. S1b). When Co-ICC/cyanuric acid ratio is further increased to 0.05, a small amount of CNTs can be observed to grow orderly on g-C$_3$N$_4$ surface (Fig. S1c). As Co-ICC dosage further increases, it becomes evident that the CNTs gradually become denser (Fig. S1d-f). In Fig. S2, Co@CNT exhibits carbon nanotube stack structure, which proves that CNTs are derived from Co-ICC. Additionally, TEM images (Fig. 2e, f and S3) further directly demonstrated that Co@CNTs grew on g-C$_3$N$_4$. Meanwhile, Co NPs were encapsulated in the tips of the CNTs, indicative of an apex growth mechanism (Fig. 2 g). This 1D CNTs array not only effectively prevents the agglomeration of Co NPs but also provides a highly efficient electron transfer pathway (Co → g-C$_3$N$_4$), facilitating the overall electron transfer efficiency. Besides, Fig. 2 h reveal the presence of abundant Co NPs with an average diameter of ca. 12.8 nm. From the high-resolution TEM (HRTEM) images (Fig. 2i), the lattice fringes with a spacing of 0.205 nm, corresponding to the (111) plane of Co metal. Meanwhile, TEM (HRTEM) images (Fig. 2i, j) confirmed the multi-walled characteristics of the CNTs. Furthermore, the hollow structure of CNTs can be observed in Fig. S3 and S4, with an outer diameter of 10–20 nm and an inner diameter of ca. 5 nm. The layer spacing of CNTs was determined to be 0.358 nm, which is in agreement with the (002) reflection of graphitic carbon, thereby confirming the high graphitization of the multi-walled CNTs grown on g-C$_3$N$_4$. Notably, the graphitic carbon layers exhibit a non-parallel orientation with respect to the axial direction of the nanotube, providing more defects and edges in the CNTs [5]. In addition, the small-scale elemental mapping analysis of Co@CNT@CN (Fig. 2k) exhibited similar outline with Fig. 2 g. Large-scale elemental mapping analysis (Fig. S5) reveals the uniform distribution of Co, C, and N elements within the Co@CNT@CN structure.

To further characterize the chemical structures, FTIR of all samples was carried out (Fig. 3a and Resources, Conceptualization, Writing – Review & Editing). The absorption bands at ~3447 cm^{-1} were attributed to N-H vibrations in all samples [33]. The broad absorption peak at 1636 cm^{-1} was attributed to the typical stretching vibration modes of C-N heterocycles [34,35]. Additionally, the weak peaks of Co@CNT@CN series samples at ~1463, ~1386, ~1322 and ~1268 cm^{-1} were ascribed to aromatic C-N stretching vibration modes (Fig. S6) [36]. The reverse peak at 805 cm^{-1} is assigned to the particular breathing mode of triazine units [37]. The ~660.7 and ~576.9 cm^{-1} bands observed in the spectrum of Co@CNT@CN-x (x = 1, 6) could be assigned to the stretching vibration peak of Co-O [38]. It was attributed to the unsuitable Co-ICC/cyanuric acid ratio (0.03 and 0.25), leading to a failure in the reduction of partial Co^{2+}. X-ray photoelectron spectra (XPS) spectra of Co@CNT@CN, displayed in Fig. 3b, further corroborate the chemical valence state and elemental composition of the composite
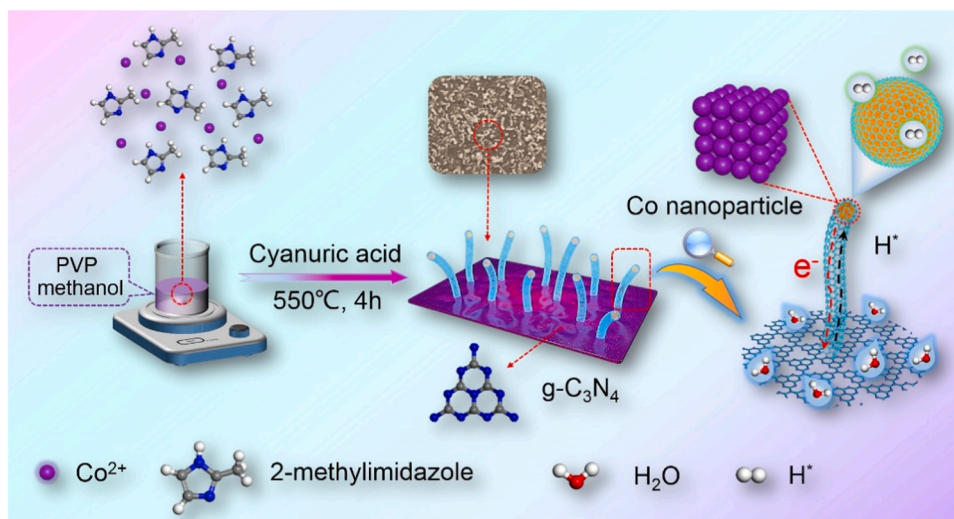
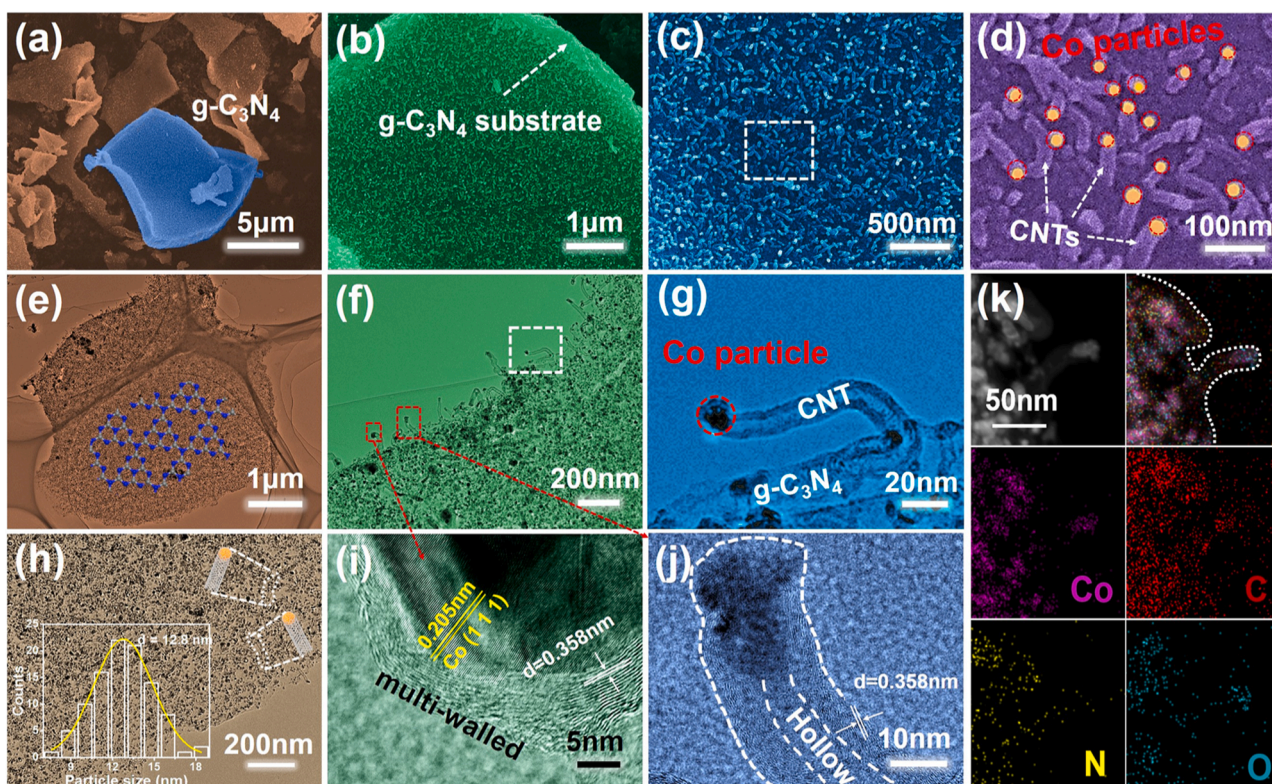**Fig. 1.** Schematic diagram of the preparation process of Co@CNT@CN.

Fig. 2. (a-d) SEM images of Co@CNT@CN. (e-h) TEM images of Co@CNT@CN, and (i, j) HRTEM images of Co@CNT@CN. (k) HADDF-STEM image and elemental mapping images of Co@CNT@CN.

electrocatalyst, with the presence of Co, C, N and O elements being evident (Fig. 3b). The Co 2p spectrum of high resolution (Fig. 3c) demonstrates two main peaks located at ≈ 778.9 and 794.7 eV, indicative of zero-valence state metallic Co. Weaker peaks positioned at 784.3 and 801.7 eV can be attributed to Co^{2+} $2p_{3/2}$ and Co^{2+} $2p_{1/2}$, respectively, which may be due to the partial oxidation of the sample exposed to air. The high-resolution C 1 s spectrum (Fig. 3d) comprises three peaks at 286.0, 284.0 and 282.9 eV, assigned to C-N, C≡N and C-C, respectively. The N 1 s spectrum in Fig. 3e, associated with three types of N configurations in g-C₃N₄, i.e., C-N = C (397.1 eV), C-N-H (398.8 eV) and π-excitation (401.9 eV), is also discernable [39].

Moreover, Fig. 3f displays the O 1 s spectrum featuring three main peaks at 528, 529.9 and 531.6 eV, originating from Co-O, O-C-O and C-OH, respectively. Besides, in comparison with pure g-C₃N₄ and CNT, it can be concluded that electrons may transfer from Co nanoparticle to CNT and g-C₃N₄ in Co@CNT@CN system. (Fig. S7) In addition, the heterostructure of Co@CNT@CN is investigated by Raman spectrum (Fig. S8). The disorderness and defect density of the carbon matrix has increased the D-band intensity and the I_D/I_G ratio increased from 0.92 to 1.02 in as-synthesized material, thereby confirming the growth of as designed Co@CNT@CN heterostructure [40,41].

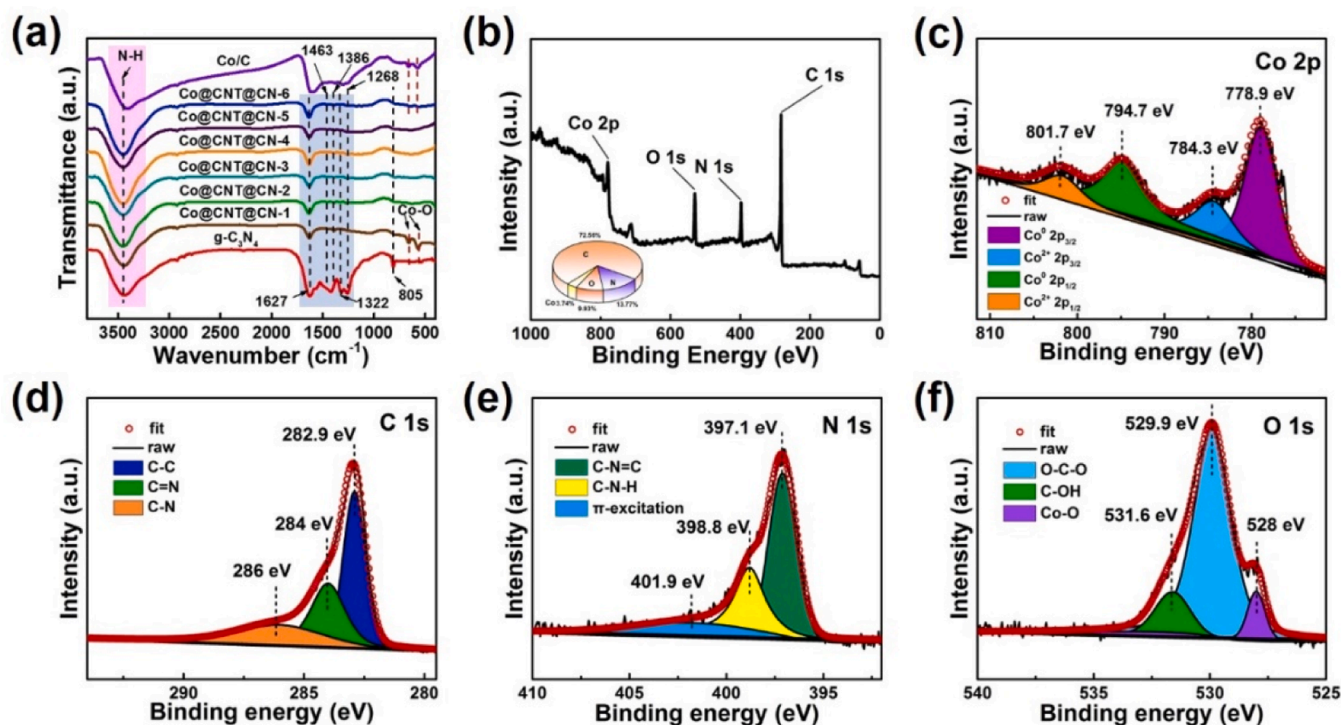X-ray diffraction (XRD) was used to characterize the crystal

Fig. 3. (a) FT-IR reflection spectra of all samples. (b) Typical XPS survey spectrum and high-resolution spectra for the Co 2p (c), C 1 s (d), N 1 s (e) and O 1 s (f).
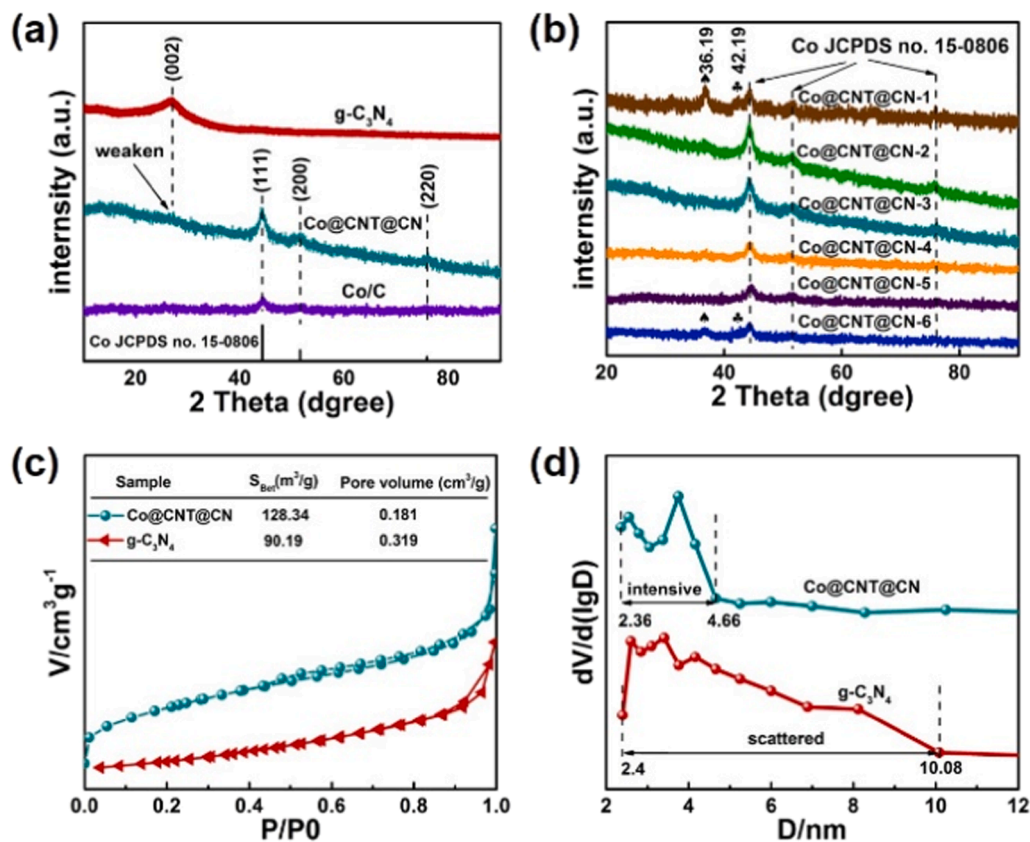

Fig. 4. (a) XRD patterns of g-C_3N_4, Co/C and Co@CNT@CN. (b) XRD patterns of Co@CNT@CN-x (x = 1, 2, 3, 4, 5, 6). (c) N_2 adsorption-desorption isotherms and (d) corresponding pore size distribution curves of Co@CNT@CN and g-C_3N_4 samples.

structures of g-C$_3$N$_4$, Co/C and all Co@CNT@CN samples (Fig. 4a). The peak located at 27.1° corresponded to the (002) plane of g-C$_3$N$_4$. Three characteristic peaks of Co/C emerged at 44.2°, 51.5°, and 75.9°, which aligned with the (111), (200), and (220) planes of Co (JCPDS No. 15–0806), respectively. It was clearly observed that Co@CNT@CN encompasses all characteristic peaks of g-C$_3$N$_4$ and cobalt, thus evidencing the successful combination of cobalt and g-C$_3$N$_4$. Compared to g-C$_3$N$_4$, the intensity of the (002) plane in Co@CNT@CN became weaker, which is likely attributed to the magnetic influence of cobalt. Additionally, Fig. 4b and S9 illustrates that all Co@CNT@CN-x (x = 1, 2, 3, 4, 5, 6) samples possess weak g-C$_3$N$_4$ peaks and Co peaks. However, it can be discerned that only Co@CNT@CN-1 and Co@CNT@CN-6 feature two obvious characteristic peaks of Co$_3$O$_4$ at 39.19° and 42.19°, which is consistent with its FTIR (Fig. 3a). The BET analysis was utilized to measure N$_2$ adsorption/desorption in both Co@CNT@CN and g-C$_3$N$_4$. As shown in Fig. 4c, the surface area (ca. 128.34 and 90.19 m^{2}g^{-1}) and pore volume (ca. 0.181 and 0.319 cm^{3}g^{-1}) of Co@CNT@CN and g-C$_3$N$_4$ were obtained. Noteworthily, the surface area of Co@CNT@CN was larger than that of g-C$_3$N$_4$, while the pore volume of Co@CNT@CN was found to be smaller. Moreover, the pore size distribution curves revealed that the pore size of Co@CNT@CN was primarily concentrated between 2.36 and 4.66 nm, while g-C$_3$N$_4$ showed a scattered aperture between 2.4 and 10.08 nm (Fig. 4d). Thus, it could be inferred that Co@CNT@CN possessed smaller and more abundant pore structure than g-C$_3$N$_4$, resulting in a larger specific surface area and improved mass transfer efficiency.

The HER electrocatalytic performance of Co@CNT@CN (Co-ICC /cyanuric acid =0.1) was evaluated in 1 M KOH solution at a scan rate of 5 mV s^{-1} via linear scan voltammetry (LSV) in a standard three-electrode configuration. As a comparative measure, commercial Pt/C (10% Pt) were also tested [42]. All reported reaction currents were corrected to account for ohmic resistance. The smaller Tafel slope meant better HER performance [43,44]. As demonstrated in Fig. 5a, Co@CNT@CN yielded a significantly lower HER overpotential of 61 mV for achieving a current density of 10 mA cm^{-2} compared to Co/C

(177 mV) and g-C$_3$N$_4$ (423 mV). These results indicated that g-C$_3$N$_4$ could significantly enhance the intrinsic catalytic kinetics of Co@CNT. This overpotential (61 mV) is lower compared to other reported catalysts, including MoS$_x$-50 @rGO/CNTs (179 mV) [45], CoSe$_2$/CNTs (190 mV) [46], NCNT/Ni–NiFe$_2$O$_4$/Ni foam (140 mV) [47], MoC-Co@CoSAs-NCNTs/CC (100 mV) [48], NiO-Ni$_{12}$P$_5$/NCNTs (170 mV) [49], WS$_{2(1-x)}$Se$_{2x}$ NTs (~260 mV) [50], and other recently reported carbon nanotube composites (Table S1), thereby proving the superior catalytic performance of Co@CNT@CN. Besides, the performance of Co@CNT@CN-x (x = 1, 2, 3, 4, 5, 6) was investigated, and Fig. S10a illustrates that the optimal performance is achieved when the Co content is 3.74 at%. The Tafel plots of Co@CNT@CN, Co/C, g-C$_3$N$_4$, and Pt/C are presented in Fig. 5b. Of particular note is the Tafel slope of Co@CNT@CN (88 mV dec^{-1}), which is significantly lower than that of Co/C (238 mV dec^{-1}) and g-C$_3$N$_4$ (525 mV dec^{-1}), indicating the dramatically enhanced HER performance of Co@CNT@CN through Volmer-Heyrovsky mechanism. The ECSA serves as a valuable measure for quantifying the surface area of electrodes, with the C$_{dl}$ method being a common approach for determining ECSA values [51]. In this study, the C$_{dl}$ values of Co@CNT@CN, Co/C, and g-C$_3$N$_4$ were determined using cyclic voltammograms (CVs) with varying scan rates (20–120 mV s^{-1}) within a non-faradic potential range (−1 to −1.1 V) in a 1 M KOH solution (Fig. S11). Based on the results presented in Fig. 5c, the capacitance values of Co@CNT@CN, Co/C, and g-C$_3$N$_4$ were found to be 34.17, 3.33, and 0.247 mF cm^{-2}, respectively, while their ECSA values were 854, 83, and 6.2 cm^{-2}, respectively. It is evident that the ordered growth of Co@CNT on g-C$_3$N$_4$ could significantly enhance its ECSA and active sites, leading to improved catalytic performance, as shown in Fig. 5d [52]. Besides, the TOF of Co@CNT@CN is 0.449 s^{-1} (η = 0.2 V in 1 M KOH). The Nyquist plots shown in Fig. 5e suggest the charge transfer resistance (R$_{ct}$, the semicircles in the higher frequency range) of Co@CNT@CN (25 Ω) was lower than that of Co@CNT (41 Ω) and g-C$_3$N$_4$. The order of the mass transfer resistance (R$_{mt}$, the semicircles in the lowest frequency range) was Co@CNT@CN (35 Ω) < Co@CNT (166 Ω) < g-C$_3$N$_4$. The stability of Co@CNT@CN was subsequently
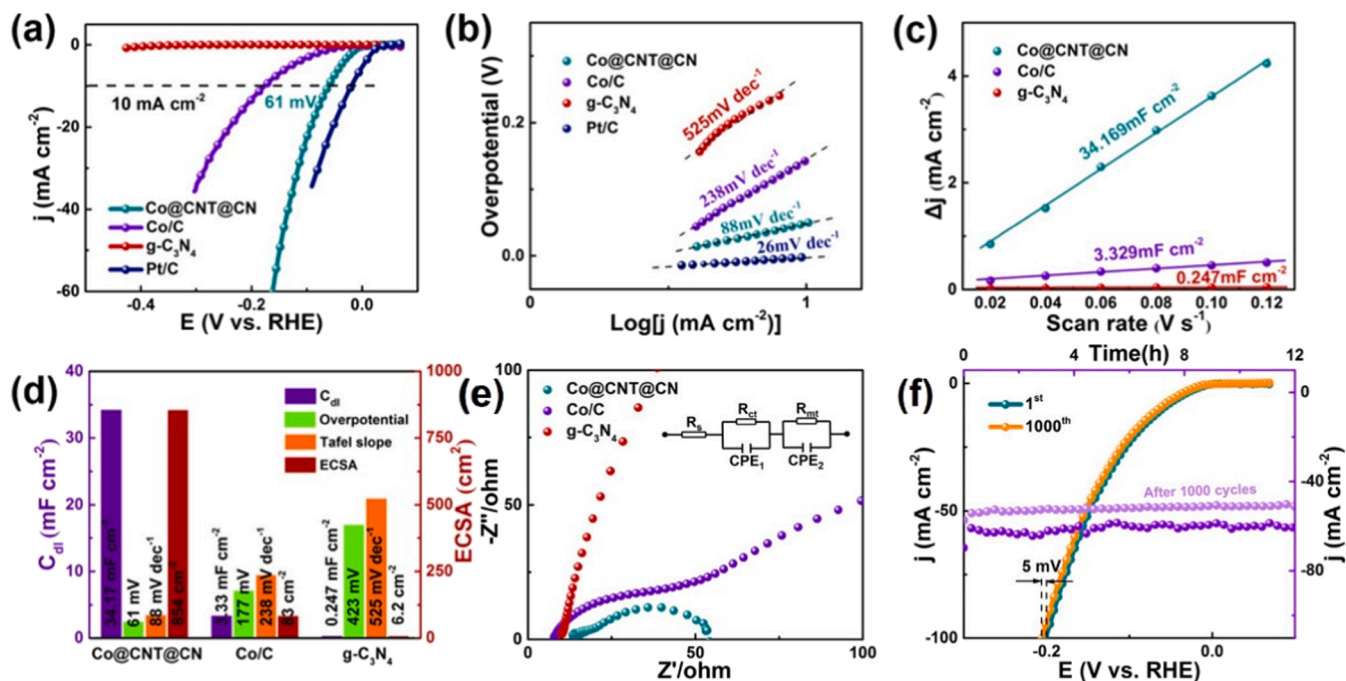

Fig. 5. (a) Polarization curves for Co@CNT@CN, Co/C, g-C$_3$N$_4$ and Pt/C in 1 M KOH with a scan rate of 5 mV s^{-1}. (b) Tafel plots for Co@CNT@CN, Co/C, g-C$_3$N$_4$, and Pt/C. (c) current density as a function of scan rate derived from CV curves of Co@CNT@CN, Co/C and g-C$_3$N$_4$. (d) Summary of double-layer capacitance (C$_{dl}$), overpotential, Tafel slope and electrochemically active surface areas (ECSA) by Co@CNT@CN, Co/C and g-C$_3$N$_4$. (e) Nyquist plots of Co@CNT@CN, Co/C and g-C$_3$N$_4$. (f) Polarization curves of Co@CNT@CN before and after 1000 CV cycles and chronoamperometric curves of Co@CNT@CN.

evaluated via continuous cyclic voltammetry scans in the potential range of -1 to -1.5 V for 1000 cycles. The current density of Co@CNT@CN only decreased by 5 mV after 1000 cycles. The current density of Co/C decreased by 23 mV after 1000 cycles (Fig. S13), and the stability is significantly lower than that of Co@CNT@CN. Therefore, g-C_3N_4 can further improve the stability of Co/CNT series catalysts. The chronoamperometric test also confirmed the excellent stability of Co@CNT@CN, as the current density remained highly consistent even after 12 h at a constant overpotential. Furthermore, Co@CNT@CN still has excellent overall stability after 1000 cycles. (Fig. 5f). SEM, XRD and XPS analysis of Co@CNT@CN after HER in alkaline electrolytes further demonstrate its structural and crystal stability (Fig. S14 and S15). Additionally, the Tafel slopes, C_{dl} and EIS of Co@CNT@CN-x (x = 1, 2, 3, 4, 5, 6) were also investigated (Fig. S10 b-d). Co@CNT@CN-3 also performed the best, which is consistent with its lowest overpotential in Fig. S7a. Notably, the overpotential of Co@CNT@CN-3 (61 mV, cyanuric acid as nitrogen source) is significantly lower than M-Co@CNT@CN-3 (375 mV, melamine as nitrogen source), demonstrating the potential application of cyanuric acid in the preparation of g-C_3N_4-based HER catalysts (Fig. S16).

The density functional theory (DFT) calculation was used to further investigate the mechanism of Co@CNT@CN in HER. A reaction pathway for alkaline HER was established, which involved the prior dissociation of H_2O (Volmer step) and the subsequent generation of H_2 (Tafel step or Heyrovsky step) [53]. It is well accepted that an optimal HER catalyst should have a ΔG_H^* close to zero. As shown in Fig. 6a, the energy barrier for breaking the H-OH bond in H_2O on Co surface was estimated to be 4.22 eV, while the dissociation energy barrier of H_2O on g-C_3N_4 surface was merely 1.2 eV. This indicates that H_2O dissociation process is facilitated on g-C_3N_4 surface. In addition, after introducing g-C_3N_4, Co@CNT@CN exhibited a more negative $E_{H_2O}^*$ (-34.63 eV) compared

to Co (119.68 eV) and Co@CNT (19.99 eV), indicating the significantly optimized H_2O adsorption capacity of Co@CNT@CN (Fig. S18). Furthermore, DFT calculations revealed that the Co surface exhibits a more favorable ΔG_H^* value (-0.13 eV) compared to g-C_3N_4 (-3.45 eV) [54]. Therefore, based on these results, it can be inferred that H_2O dissociation is more likely to occur on the g-C_3N_4 surface, while the combination of H* to form H_2 is much easier on Co nanoparticle surfaces. In Fig. 6b, after introducing g-C_3N_4, the free energy changes from -0.48 eV (Co@CNT) to -0.13 eV (Co@CNT@CN, close to 0 eV), indicating the unique performance optimization effect of g-C_3N_4. Similarly, Co@CNT presents better free energy of -0.48 eV than Co (-1.4 eV), proving that CNT is favorable for the combination of H* to form H_2 (Fig. S19). The charge density difference and electrostatic potential of Co@CNT@CN were examined, as depicted in Fig. 6c and Fig. S20. The results indicate that electrons transfer tend of Co → N-CNT → g-C_3N_4, and accumulate near g-C_3N_4, thus forming a rich electron environment. In addition, the corresponding slices (Fig. S21) of Co@CNT@CN show the same electrons transfer tendency and electrons distribution. The accumulation of electrons on g-C_3N_4 surface is conducive to the splitting of adsorbed H_2O molecules, which is consistent with its H_2O dissociation function. Fig. S22 provides the projected density of states (PDOS) of H_2O, wherein the orbital energies (1_{a1}, 2_{a1}, 1_{b2}, 3_{a1}, 1_{b1}, 4_{a1} and 2_{b2}) of H_2O on Co@CNT@CN, g-C_3N_4 and Co@CNT exhibit notable left shift relative to free H_2O. The lower orbital energy below the Fermi level (0 eV) could accelerate the migration of e⁻ from Co@CNT@CN to H_2O, leading to e⁻ accumulation on H_2O. Notably, when introducing Co@CNT in g-C_3N_4, the orbital energies of H_2O shift very obviously, implying that Co@CNT plays the key role in e⁻ accelerates migration [55]. Fig. 6d clearly reveals that the Fermi level of Co@CNT@CN is raised compared to Co@CNT, indicating that g-C_3N_4 can stimulate more electrons to participate in the HER process. Besides,
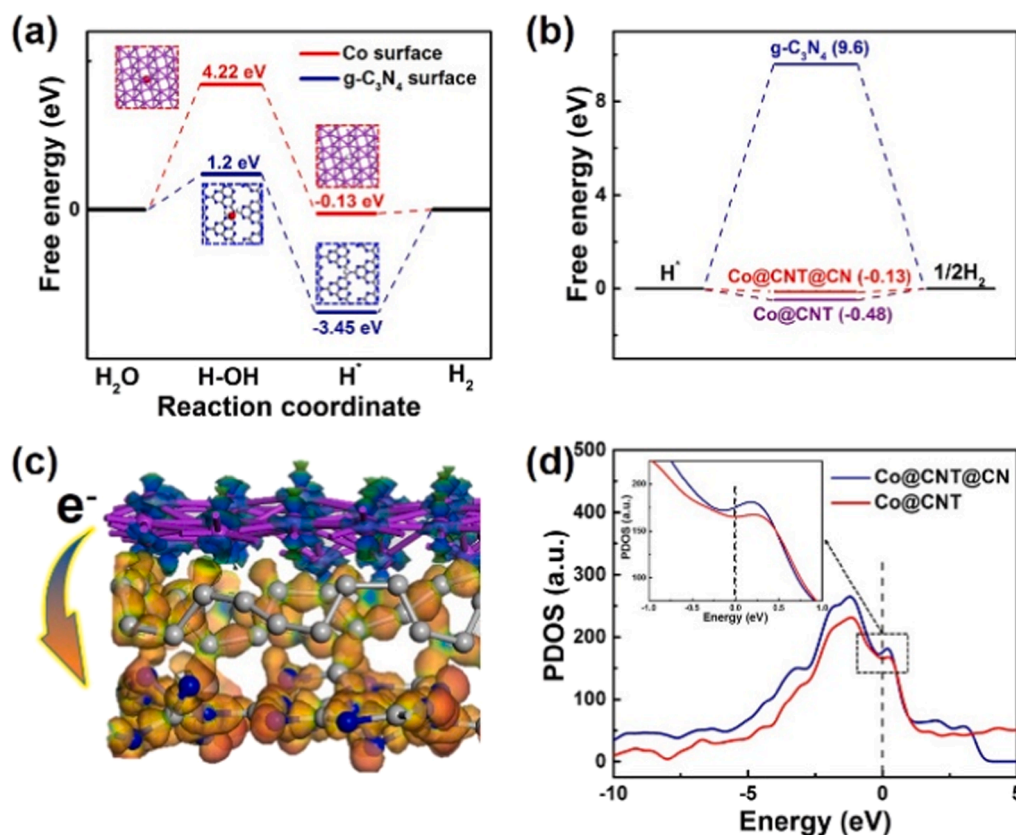

Fig. 6. (a) The corresponding free energy diagram for HER on Co and g-C_3N_4 surface. (b) The free energy diagram for HER on Co@CNT, g-C_3N_4 and Co@CNT@CN. (c) Charge density difference model of Co@CNT@CN. (d) The projected density of states (PDOS) for Co@CNT@CN and Co@CNT. The Co C N atoms are represented by purple, gray and blue spheres, respectively.

absorbed H_2O on Co@CNT is increased from 0.975 to 0.987 Å. After introducing g-C_3N_4 in Co@CNT, the H-O bond is further augmented to 1.002 Å, which directly proves the excellent splitting H_2O of Co@CNT@CN (Fig. S23). Moreover, when H_2O was adsorbed on Co@CNT@CN, the charge of H atom in H_2O change from 0.530 to 0.420, indicating the excellent H_2O excitation function of Co@CNT@CN as well.

The HER performances for Co@CNT@CN, Co/C, g-C_3N_4, and Pt/C were also tested in 0.5 M H_2SO_4 and 1.0 M PBS, respectively. Fig. 7a illustrates the HER performance of Co@CNT@CN, Co/C, g-C_3N_4, and Pt/C in 0.5 M H_2SO_4. Co@CNT@CN displays an overpotential of 145 mV for a current density of 10 mA cm^{-2}, surpassing that of Co/C (357 mV) and g-C_3N_4 (492 mV). It compares favorably to the behaviors of CoP-CNT/NG (155 mV) [56], EDA-MWCNTs (600 mV) [57], Ni-CNTs (261 mV) [58], CoS_2/MoS_2 @N-rGO-MWCNT (281 mV) [59], and some other carbon nanotube composites catalysts (Table S2), thereby proving the higher catalytic efficiency of Co@CNT@CN. The Tafel slope of Co@CNT@CN (134 mV dec^{-1}) is lower than that of Co/C (185 mV dec^{-1}) and g-C_3N_4 (216 mV dec^{-1}), highlighting its superior electrocatalytic activity towards HER. In addition, the Co@CNT@CN electrode demonstrates excellent long-term durability for the HER in 0.5 M H_2SO_4 (Fig. 7c). Co@CNT@CN demonstrated exceptional HER performance in 1.0 M PBS, exhibiting an overpotential of only 170 mV to drive a current density of 10 mA cm^{-2} (Fig. 7d). This performance surpasses that of Co/C (417 mV), g-C_3N_4 (>800 mV), and those of other reported catalysts, including $Fe_{0.4}Co_{0.6}$-NCNTs (202 mV) [60], MoS_2/-Co_9S_8/rGO-CNTs (176 mV) [61], Mo/Mo_2C/N-CNFs (294 mV) [62], and some other carbon catalysts in neutral condition (Table S3). The Tafel slope of Co@CNT@CN was measured to be 165 mV dec^{-1}, substantially lower than that of Co/C (356 mV dec^{-1}) and g-C_3N_4 (620 mV dec^{-1}) (Fig. 7e). The overpotential and Tafel slope of Co@CNT@CN indicate its excellent catalytic performance in PBS solution. Meanwhile, Co@CNT@CN demonstrated excellent stability under neutral conditions (Fig. 7 f). Besides, the TOF of Co@CNT@CN in 1 M PBS and

0.5 M H_2SO_4 are 0.062 s^{-1} ($\eta = 0.2$ V) and 0.131 s^{-1} ($\eta = 0.2$ V), respectively Furthermore, the overpotential, Tafel slopes and stability of Co@CNT@CN-x (x = 1, 2, 3, 4, 5, 6) was also evaluated in 0.5 M H_2SO_4 and 1.0 M PBS solutions (Fig. S24). XRD and XPS analysis of Co@CNT@CN after HER in acidic and neutral electrolytes further demonstrate its crystal stability. (Fig. S25 and S26).

Finally, based on the DFT computational results and the Volmer-Heyrovsky process, we propose a feasible HER mechanism in alkaline media (Fig. 8). The calculated pathway for electron transfer occurred as follows: Co → CNTs → g-C_3N_4·H_2O tend to adsorb g-C_3N_4 surface. The accumulation of electrons on g-C_3N_4 further activates the surrounding H_2O molecules. As a result of electron activation, the H-O bonds in H_2O are extended, facilitating the dissociation of H_2O molecules into H atoms and OH^-. Therefore, the Volmer reaction primarily
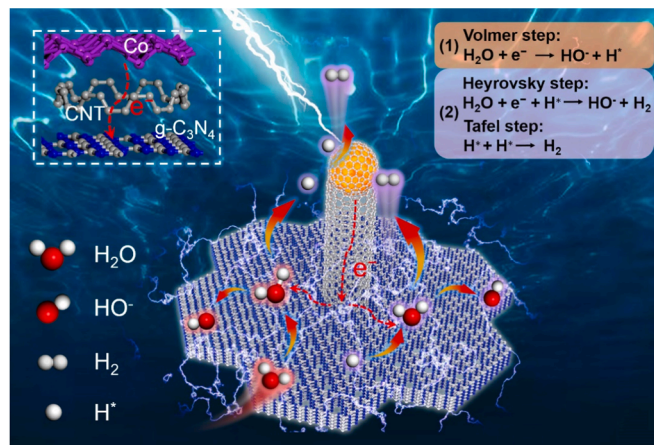

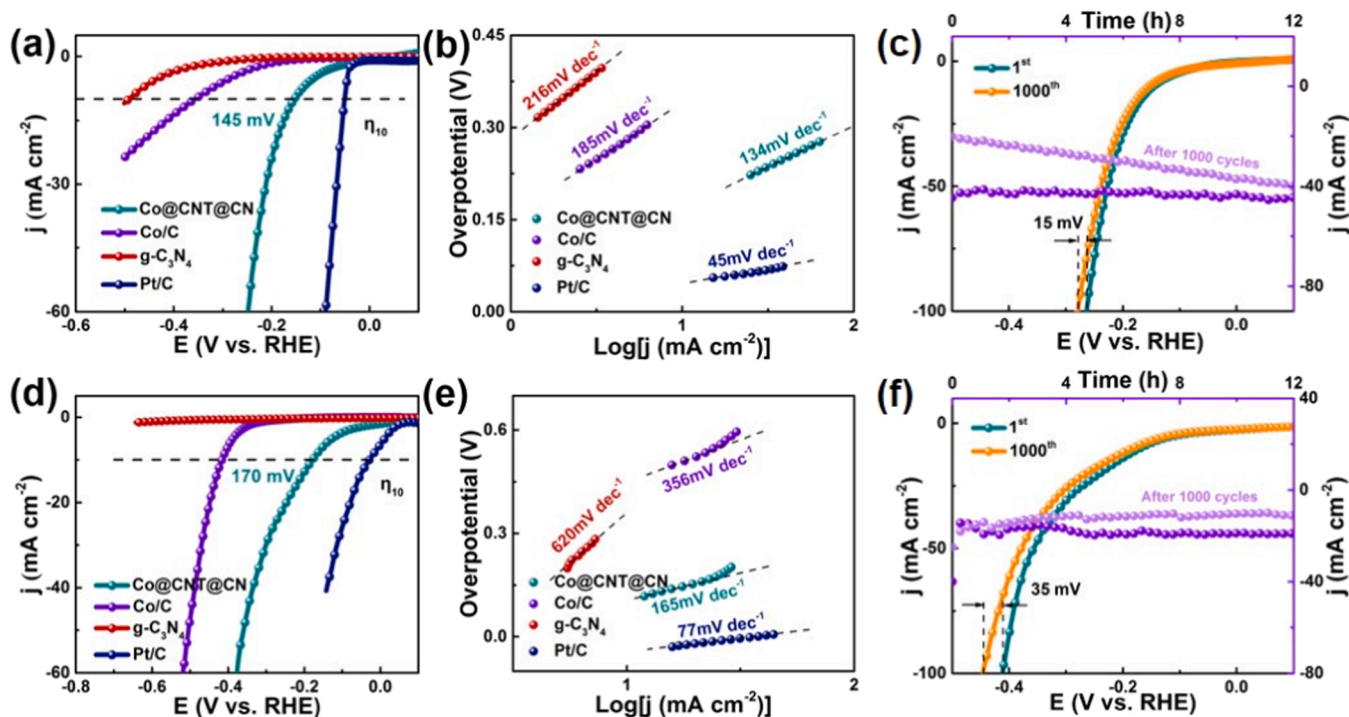**Fig. 8.** Diagram of reaction mechanism of Co@CNT@CN under electrocatalytic hydrogen evolution.

Fig. 7. Test condition: 0.5 M H_2SO_4 solution. (a) HER polarization curves of Co@CNT@CN, Co/C, g-C_3N_4, and Pt/C; (b) Tafel plots for Co@CNT@CN, Co/C, g-C_3N_4, and Pt/C; (c) Polarization curves of Co@CNT@CN before and after 1000 CV cycles and chronoamperometric curves of Co@CNT@CN. Test condition: 1.0 M PBS solution. (d) HER polarization curves of Co@CNT@CN, Co/C, g-C_3N_4, and Pt/C; (e) Tafel plots of Co@CNT@CN, Co/C, g-C_3N_4, and Pt/C; (f) Polarization curves of Co@CNT@CN before and after 1000 CV cycles and chronoamperometric curves of Co@CNT@CN.

occurs on g-C$_3$N$_4$ (Volmer step: H$_2$O + e$^-$ → H* + OH$^-$). Subsequently, the generated H* can combined to form H$_2$ through either the Heyrovsky or Tafel steps. The computational results indicate that H* is easier to combine on Co NPs. Therefore, according to the Volmer-Heyrovsky theory, a portion of H* transfers to Co NPs to form H$_2$ (Tafel step: H*+ H*→H$_2$), while another portion combines with H$_2$O and electrons to produce H$_2$ and OH$^-$ (Heyrovsky step: H*+ H$_2$O +e$^-$ → OH$^-$+H$_2$).

4. Conclusion

In summary, we developed a novel Co@N-CNT@g-C$_3$N$_4$ electrocatalyst via a simple coordination-polymerization integrated strategy. Co nanoparticles were encapsulated in the tip of carbon nanotubes and carbon nanotubes grew on g-C$_3$N$_4$ to bridge Co particles and g-C$_3$N$_4$. Co NPs acted as abundant active sites, while CNTs provided efficient and stable electron transfer pathway. Moreover, the introduction of g-C$_3$N$_4$ not only enhanced the overall electroconductivity, but also improved the stability. Specifically, Co@CNT@CN exhibited remarkable catalytic activity and stability at all pH values, requiring overpotentials of only 61, 145, and 170 mV to achieve a current density of 10 mA cm^{-2} in 1 M KOH, 0.5 M H$_2$SO$_4$ and 1.0 M PBS, respectively. Meanwhile, other electrochemical properties (Tafel slopes, EIS and ECSA) were also excellent. The ΔG_{H*} of Co@CNT@CN was only − 0.13 eV, which was conducive to H$_2$ formation. DFT calculations revealed that electrons transfer tend of Co → N-CNT → g-C$_3$N$_4$. The accumulation of electrons on g-C$_3$N$_4$ extends the O-H of H$_2$O from 0.975 to 1.002 Å. Simultaneously, the charge of H atom in H$_2$O change from 0.530 to 0.420, demonstrating directly the HER enhancement of Co@CNT@CN. This study points out new directions for the design and development of integrated transition metal-based/carbon nanotubes/g-C$_3$N$_4$ materials.

CRediT authorship contribution statement

Xiang Yan: Methodology, Data curation, Software, Writing – draft preparation, Visualization, Investigation. **Chao Zhang:** Conceptualization, Resources, Funding acquisition, Writing – review & editing. **Jinguang Hu:** Supervision, Validation. **Yuming Zhou:** Software, Supervision. **Zhiguo Lv:** Resources, Conceptualization, Writing – review & editing.

Declaration of Competing Interest

The authors declare that they have no known competing financial interests or personal relationships that could have appeared to influence the work reported in this paper.

Data availability

Data will be made available on request.

Acknowledgements

References

[1] N. Logeshwaran, S. Ramakrishnan, S.S. Chandrasekaran, M. Vinothkannan, A. R. Kim, S. Sengodan, D.B. Velusamy, P. Varadhan, J.-H. He, D.J. Yoo, An efficient and durable trifunctional electrocatalyst for zinc–air batteries driven overall water splitting, Appl. Catal. B 297 (2021), 120405.

[2] J. Lee, H. Jung, Y.S. Park, N. Kwon, S. Woo, N.C.S. Selvam, G.S. Han, H.S. Jung, P. J. Yoo, S.M. Choi, J.W. Han, B. Lim, Chemical transformation approach for high-performance ternary NiFeCo metal compound-based water splitting electrodes, Appl. Catal. B 294 (2021), 120246.

[3] W. Zhu, X. Fu, A. Wang, M. Ren, Z. Wei, C. Tang, X. Sun, J. Wang, Energy-efficient electrolytic H$_2$ production and high-value added H$_2$-acid-base co-electrosynthesis modes enabled by a Ni$_2$P catalyst in a diaphragm cell, Appl. Catal. B 317 (2022), 121726.

[4] Y. Feng, Z. Li, C.-Q. Cheng, W.-J. Kang, J. Mao, G.-R. Shen, J. Yang, C.-K. Dong, H. Liu, X.-W. Du, Strawberry-like Co$_3$O$_4$-Ag bifunctional catalyst for overall water splitting, Appl. Catal. B 299 (2021), 120658.

[5] T. Li, S. Li, Q. Liu, J. Yin, D. Sun, M. Zhang, L. Xu, Y. Tang, Y. Zhang, Immobilization of Ni$_3$Co nanoparticles into N-doped carbon nanotube/nanofiber integrated hierarchically branched architectures toward efficient overall water splitting, Adv. Sci. 7 (2019) 1902371.

[6] Y. Chen, D. Sun, L. Du, Y. Jiao, W. Han, G. Tian, Sandwich-structured hybrid of NiCo nanoparticles-embedded carbon nanotubes grafted on C$_3$N$_4$ nanosheets for efficient photodehydrogenative coupling reactions, ACS Appl. Mater. Interfaces 14 (2022) 24425–24434.

[7] Z.-J. Jiang, G. Xie, L. Guo, J. Huang, Z. Jiang, Co nanoparticles coupling induced high catalytic activity of nitrogen doped carbon towards hydrogen evolution reaction in acidic/alkaline solutions, Electrochim. Acta 342 (2020), 136076.

[8] Z. Wu, B. Liu, H. Jing, H. Gao, B. He, X. Xia, W. Lei, Q. Hao, Porous carbon framework decorated with carbon nanotubes encapsulating cobalt phosphide for efficient overall water splitting, J. Colloid Interface Sci. 629 (2023) 22–32.

[9] D. Wang, M. Al-Mamun, W. Gong, Y. Lv, C. Chen, Y. Lin, G. Wang, H. Zhang, H. Zhao, Converting Co^{2+}-impregnated g-C$_3$N$_4$ into N-doped CNTs-confined Co nanoparticles for efficient hydrogenation rearrangement reactions of furanic aldehydes, Nano Res. 14 (2021) 2846–2852.

[10] Y. Li, M. Cui, T. Li, Y. Shen, Z. Si, H. Wang, Embedding Co$_2$P nanoparticles into co-doped carbon hollow polyhedron as a bifunctional electrocatalyst for efficient overall water splitting, Int. J. Hydrog. Energy 45 (2020) 16540–16549.

[11] K. An, X. Xu, Mo$_2$C based electrocatalyst with nitrogen doped three-dimensional mesoporous carbon as matrix, synthesis and HER activity study, Electrochim. Acta 293 (2019) 348–355.

[12] R.A. Araujo, A.F. Rubira, T. Asefa, R. Silva, Metal doped carbon nanoneedles and effect of carbon organization with activity for hydrogen evolution reaction (HER), Carbohydr. Polym. 137 (2016) 719–725.

[13] S. Riyajuddin, K. Azmi, M. Pahuja, S. Kumar, T. Maruyama, C. Bera, K. Ghosh, Super-hydrophilic hierarchical Ni-foam-graphene-carbon nanotubes-Ni$_2$P–CuP$_2$ nano-architecture as efficient electrocatalyst for overall water splitting, ACS Nano 15 (2021) 5586–5599.

[14] G. Zhang, P. Wang, W.T. Lu, C.Y. Wang, Y.K. Li, C. Ding, J. Gu, X.S. Zheng, F. F. Cao, Co nanoparticles/Co, N, S Tri-doped graphene templated from in-situ-formed Co, S Co-doped g-C$_3$N$_4$ as an active bifunctional electrocatalyst for overall water splitting, ACS Appl. Mater. Interfaces 9 (2017) 28566–28576.

[15] B.J. Ferraz, J. Kong, B. Li, N. Neng Tham, C. Blackman, Z. Liu, Co/N nanoparticles supported on a C$_3$N$_4$/polydopamine framework as a bifunctional electrocatalyst for rechargeable zinc-air batteries, J. Electroanal. Chem. 921 (2022) 116702.

[16] P. Sabhapathy, I. Shown, A. Sabbah, P. Raghunath, J.-L. Chen, W.-F. Chen, M.-C. Lin, K.-H. Chen, L.-C. Chen, Electronic structure modulation of isolated Co-N$_4$ electrocatalyst by sulfur for improved pH-universal hydrogen evolution reaction, Nano Energy 80 (2021), 105544.

[17] C. Chen, M. Wen, T. Cheng, Y. Tian, X. Zhang, B. Hou, Accessible active sites activated by nano cobalt antimony oxide @ carbon nanotube composite electrocatalyst for highly enhanced hydrogen evolution reaction, Int. J. Hydrog. Energy 48 (2023) 7719–7736.

[18] Z. Yu, K. Yao, S. Zhang, Y. Liu, Y. Sun, W. Huang, N. Hu, Morphological and reactive optimization of g-C$_3$N$_4$-derived Co,N-codoped carbon nanotubes for hydrogen evolution reaction, N. J. Chem. 45 (2021) 6308–6314.

[19] S. Zhang, X. Xiao, T. Lv, X. Lv, B. Liu, W. Wei, J. Liu, Cobalt encapsulated N-doped defect-rich carbon nanotube as pH universal hydrogen evolution electrocatalyst, Appl. Surf. Sci. 446 (2018) 10–17.

[20] C. Zhou, X. Han, F. Zhu, X. Zhang, Y. Lu, J. Lang, X. Cao, H. Gu, Facile synthesis of the encapsulation of Co-based multimetallic alloys/oxide nanoparticles nirtogen-doped carbon nanotubes as electrocatalysts for the HER/OER, Int. J. Hydrog. Energy 47 (2022) 27775–27786.

[21] Z. Li, K. Wang, X. Tan, X. Liu, G. Wang, G. Xie, L. Jiang, Defect-enriched multistage skeleton morphology Ni-Fe-P-Ni$_3$S$_2$ heterogeneous catalyst on Ni foam for efficient overall water splitting, Chem. Eng. J. 424 (2021), 130390.

[22] X. Zhang, K. Matras-Postolek, P. Yang, S.P. Jiang, Pt clusters in carbon network to enhance photocatalytic CO$_2$ and benzene conversion of WOx/g-C$_3$N$_4$ nanosheets, Carbon 214 (2023).

[23] X. Zhang, K. Matras-Postolek, P. Yang, S. Ping Jiang, Z-scheme WOx/Cu-g-C$_3$N$_4$ heterojunction nanoarchitectonics with promoted charge separation and transfer towards efficient full solar-spectrum photocatalysis, J. Colloid Interface Sci. 636 (2023) 646–656.

[24] X. Zhang, S.P. Jiang, Layered g-C$_3$N$_4$/TiO$_2$ nanocomposites for efficient photocatalytic water splitting and CO$_2$ reduction: a review, Mater. Today Energy 23 (2022).

[25] X. Zhang, K. Matras-Postolek, P. Yang, Heterojunction nanoarchitectonics of WOx/Au-g-C$_3$N$_4$ with efficient photogenerated carrier separation and transfer toward improved NO and benzene conversion, Mater. Today Adv. 17 (2023).

[26] Q. Liu, C. Zeng, Z. Xie, L. Ai, Y. Liu, Q. Zhou, J. Jiang, H. Sun, S. Wang, Cobalt@ nitrogen-doped bamboo-structured carbon nanotube to boost photocatalytic hydrogen evolution on carbon nitride, Appl. Catal. B 254 (2019) 443–451.

[27] H. Niu, W. Zhao, H. Lv, Y. Yang, Y. Cai, Accurate design of hollow/tubular porous g-C₃N₄ from melamine-cyanuric acid supramolecular prepared with mechanochemical method, Chem. Eng. J. 411 (2021), 128400.

[28] M. Shalom, S. Inal, C. Fettkenhauer, D. Neher, M. Antonietti, Improving carbon nitride photocatalysis by supramolecular preorganization of monomers, J. Am. Chem. Soc. 135 (2013) 7118–7121.

[29] Q. Liu, X. Wang, Q. Yang, Z. Zhang, X. Fang, Mesoporous g-C₃N₄ nanosheets prepared by calcining a novel supramolecular precursor for high-efficiency photocatalytic hydrogen evolution, Appl. Surf. Sci. 450 (2018) 46–56.

[30] X. Zhang, X. Zhang, P. Yang, S.P. Jiang, Layered graphitic carbon nitride: nano-heterostructures, photo/electro-chemical performance and trends, J. Nanostructure Chem. 12 (2021) 669–691.

[31] Y. Liu, X. Guo, Z. Chen, W. Zhang, Y. Wang, Y. Zheng, X. Tang, M. Zhang, Z. Peng, R. Li, Y. Huang, Microwave-synthesis of g-C₃N₄ nanoribbons assembled seaweed-like architecture with enhanced photocatalytic property, Appl. Catal. B 266 (2020), 118624.

[32] Z. Huang, Y. Zhang, H. Dai, Y. Wang, C. Qin, W. Chen, Y. Zhou, S. Yuan, Highly dispersed Pd nanoparticles hybridizing with 3D hollow-sphere g-C₃N₄ to construct 0D/3D composites for efficient photocatalytic hydrogen evolution, J. Catal. 378 (2019) 331–340.

[33] S. Zhao, Y. Zhang, Y. Wang, Y. Zhou, K. Qiu, C. Zhang, J. Fang, X. Sheng, Ionic liquid-assisted synthesis of Br-modified g-C₃N₄ semiconductors with high surface area and highly porous structure for photoredox water splitting, J. Power Sources 370 (2017) 106–113.

[34] S.L. Zhao, Y, Y. Wang, J. Fang, Y. Qi, Y. Zhou, L. Liu, S. Zhuo, A self-assembly strategy to synthesize carbon doped carbon nitride microtubes with a large π-electron conjugated system for efficient H2 evolution, Chem. Eng. J. 447 (2022), 137436.

[35] Y. Chen, W. Huang, D. He, Y. Situ, H. Huang, Construction of heterostructured g-C₃N₄/Ag/TiO₂ microspheres with enhanced photocatalysis performance under visible-light irradiation, ACS Appl. Mater. Interfaces 6 (2014) 14405–14414.

[36] L. Gu, J. Wang, Z. Zou, X. Han, Graphitic-C₃N₄-hybridized TiO₂ nanosheets with reactive 001 facets to enhance the UV- and visible-light photocatalytic activity, J. Hazard. Mater. 268 (2014) 216–223.

[37] Y. Liu, S. Zhao, C. Zhang, J. Fang, L. Xie, Y. Zhou, S. Zhuo, Hollow tubular carbon doping graphitic carbon nitride with adjustable structure for highly enhanced photocatalytic hydrogen production, Carbon 182 (2021) 287–296.

[38] C. Zhang, Y. Liu, J. Wang, W. Li, Y. Wang, G. Qin, Z. Lv, A well-designed fencelike Co₃O₄@MoO₃ derived from Co foam for enhanced electrocatalytic HER, Appl. Surf. Sci. 595 (2022), 153532.

[39] X. Zhang, X. Ran Zhang, P. Yang, H.-S. Chen, S. Ping, Jiang, Black magnetic Cu-g-C₃N₄ nanosheets towards efficient photocatalytic H₂ generation and CO₂/benzene conversion, Chem. Eng. J. 450 (2022).

[40] S. Riyajuddin, M. Pahuja, P.K. Sachdeva, S. Azmi, S. Kumar, M. Afshan, F. Ali, J. Sultana, T. Maruyama, C. Bera, K. Ghosh, Super-hydrophilic leaflike Sn₄P₃ on the porous seamless graphene–carbon nanotube heterostructure as an efficient electrocatalyst for solar-driven overall water splitting, ACS Nano 16 (2022) 4861–4875.

[41] M. Pahuja, I. De, S.A. Siddiqui, S. Das, M. Afshan, K. Alam, S. Riyajuddin, S. Rani, R. Ghosh, D. Rani, K. Gill, M. Singh, K. Ghosh, Seamless architecture of porous carbon matrix decorated with Ta₂O₅ nanostructure-based recyclable photocatalytic cartridge for toxicity remediation of industrial dye effluents, Sep. Purif. Technol. 320 (2023).

[42] G.S. Jamila, S. Sajjad, S.A.K. Leghari, T. Kallio, C. Flox, Glucose derived carbon quantum dots on tungstate-titanate nanocomposite for hydrogen energy evolution and solar light catalysis, J. Nanostructure Chem. 12 (2021) 611–623.

[43] S.W. Sun, G.F. Wang, Y. Zhou, F.B. Wang, X.H. Xia, High-performance Ru@C₄N electrocatalyst for hydrogen evolution reaction in both acidic and alkaline solutions, ACS Appl. Mater. Interfaces 11 (2019) 19176–19182.

[44] W. Zhao, C. Luo, Y. Lin, G.-B. Wang, H.M. Chen, P. Kuang, J. Yu, Pt–Ru dimer electrocatalyst with electron redistribution for hydrogen evolution reaction, ACS Catal. 12 (2022) 5540–5548.

[45] Y. Guo, R. Wang, X. Xu, Y. Shang, B. Gao, Three-dimensional reduced graphene oxide/carbon nanotube nanocomposites anchoring of amorphous and crystalline molybdenum sulfide: physicochemical characteristics and electrocatalytic hydrogen evolution performances, Electrochim. Acta 273 (2018) 402–411.

[46] G. Wei, K. Du, X. Zhao, J. Wang, W. Yan, C. An, C. An, Cable-like carbon nanotubes decorated metal-organic framework derived ultrathin CoSe₂/CNTs nanosheets for electrocatalytic overall water splitting, Chin. Chem. Lett. 31 (2020) 2641–2644.

[47] Q. Qin, L. Chen, T. Wei, Y. Wang, X. Liu, Ni/NiM₂O₄ (M = Mn or Fe) supported on N-doped carbon nanotubes as trifunctional electrocatalysts for ORR, OER and HER, Catal. Sci. Technol. 9 (2019) 1595–1601.

[48] Y. Cheng, J. Gong, B. Cao, X. Xu, P. Jing, B. Liu, R. Gao, J. Zhang, An ingenious strategy to integrate multiple electrocatalytically active components within a well-aligned nitrogen-doped carbon nanotube array electrode for electrocatalysis, ACS Catal. 11 (2021) 3958–3974.

[49] Y. Zhang, Y. Tan, X. Wang, L. Dong, A. Liu, Hybrid of NiO-Ni₁₂P₅/N-doped carbon nanotubes as non-noble electrocatalyst for efficient hydrogen evolution reaction, Colloids Surf. A Physicochem. Eng. Asp. 608 (2021) 125613.

[50] F.W. Kai Xu, Zhenxing Wang, Xueying Zhan, Qisheng Wang, Zhongzhou Cheng, Muhammad Safdar, Jun He, Component-controllable WS₂(₁₋ₓ)Se₂ₓ nanotubes for efficient hydrogen evolution reaction, ACS Nano 8 (2014) 8468–8476.

[51] Y. Chen, G. Yu, W. Chen, Y. Liu, G.D. Li, P. Zhu, Q. Tao, Q. Li, J. Liu, X. Shen, H. Li, X. Huang, D. Wang, T. Asefa, X. Zou, Highly active, nonprecious electrocatalyst comprising borophene subunits for the hydrogen evolution reaction, J. Am. Chem. Soc. 139 (2017) 12370–12373.

[52] S. Nong, W. Dong, J. Yin, B. Dong, Y. Lu, X. Yuan, X. Wang, K. Bu, M. Chen, S. Jiang, L.M. Liu, M. Sui, F. Huang, Well-dispersed ruthenium in mesoporous crystal TiO₂ as an advanced electrocatalyst for hydrogen evolution reaction, J. Am. Chem. Soc. 140 (2018) 5719–5727.

[53] B. Zhang, J. Liu, J. Wang, Y. Ruan, X. Ji, K. Xu, C. Chen, H. Wan, L. Miao, J. Jiang, Interface engineering: the Ni(OH)₂ /MoS₂ heterostructure for highly efficient alkaline hydrogen evolution, Nano Energy 37 (2017) 74–80.

[54] H. Duan, D. Li, Y. Tang, Y. He, S. Ji, R. Wang, H. Lv, P.P. Lopes, A.P. Paulikas, H. Li, S.X. Mao, C. Wang, N.M. Markovic, J. Li, V.R. Stamenkovic, Y. Li, High-performance Rh₂P electrocatalyst for efficient water splitting, J. Am. Chem. Soc. 139 (2017) 5494–5502.

[55] H. Wang, C. Qian, J. Liu, Y. Zeng, D. Wang, W. Zhou, L. Gu, H. Wu, G. Liu, Y. Zhao, Integrating suitable linkage of covalent organic frameworks into covalently bridged inorganic/organic hybrids toward efficient photocatalysis, J. Am. Chem. Soc. 142 (2020) 4862–4871.

[56] X. Guan, J. Ma, K. Li, J. Liang, Z. Li, W. Peng, G. Zhang, X. Fan, F. Zhang, Y. Li, Multilevel N-doped carbon nanotube/graphene supported cobalt phosphide nanoparticles for electrocatalytic hydrogen evolution reaction, Int. J. Hydrog. Energy 44 (2019) 30053–30061.

[57] S.S. Narwade, S.M. Mali, B.R. Sathe, Amine-functionalized multi-walled carbon nanotubes (EDA-MWCNTs) for electrochemical water splitting reactions, N. J. Chem. 45 (2021) 3932–3939.

[58] B. Thangavel, S. Berchmans, G. Venkatachalam, Ni@carbon nanotubes derived from Ni-MOF as a superior electrocatalyst for hydrogen evolution reaction in acidic medium, Energy Fuels 35 (2020) 1866–1873.

[59] B.N. Darshan, A. Kareem, T. Maiyalagan, V. Edwin Geo, CoS₂/MoS₂ decorated with nitrogen doped reduced graphene oxide and multiwalled carbon nanotube 3D hybrid as efficient electrocatalyst for hydrogen evolution reaction, Int. J. Hydrog. Energy 46 (2021) 13952–13959.

[60] Z. Wang, S. Zhang, X. Lv, J. Bai, W. Yu, J. Liu, Electrocatalytic hydrogen evolution on iron-cobalt nanoparticles encapsulated in nitrogenated carbon nanotube, Int. J. Hydrog. Energy 44 (2019) 16478–16486.

[61] M. Wang, K. Jian, Z. Lv, D. Li, G. Fan, R. Zhang, J. Dang, MoS₂/Co₉S₈/MoC heterostructure connected by carbon nanotubes as electrocatalyst for efficient hydrogen evolution reaction, J. Mater. Sci. Technol. 79 (2021) 29–34.

[62] M. Li, H. Wang, Y. Zhu, D. Tian, C. Wang, X. Lu, Mo/Mo₂C encapsulated in nitrogen-doped carbon nanofibers as efficiently integrated heterojunction electrocatalysts for hydrogen evolution reaction in wide pH range, Appl. Surf. Sci. 496 (2019), 143672.